Chemical Science

Accepted Manuscript

This article can be cited before page numbers have been issued, to do this please use: J. Wang, S. Fan, W. Yuan, Y. Wang and Q. Zhai, *Chem. Sci.*, 2025, DOI: 10.1039/D5SC02144H.

ROYAL SOCIETY OF CHEMISTRY

rsc.li/chemical-science

View Article Online
DOI: 10.1039/D5SC02144H

ARTICLE

Inter-Cluster-Linker-Absence-Enabled Sub-Ångstrom Pore Modulation in Metal-Organic Framework for Multi-Scenario CO_2 Capture

Received 00th January 20xx,
Accepted 00th January 20xx

DOI: 10.1039/x0xx00000x

Jia-Wen Wang, Shu-Cong Fan, Wenyu Yuan, Ying Wang, and Quan-Guo Zhai*

Ultrafine aperture control of carbon capture adsorbents is first and foremost important but inscrutable. Herein an inter-cluster-linker-absence-enabled sub-Ångstrom pore modulation strategy is proposed through the efficient transitivity of coordination bonds in metal-organic framework (MOF). The feasibility of this strategy is well-demonstrated in SNNU-98-M materials composed of directly-connected $[M_8(TAZ)_9]$ (M = Cd or Cu, TAZ = tetrazolate) triangular prism clusters. The removal of inter-cluster linkers effectively transfers the difference of coordination bond length (~2.3 Å for Cd(II)-N and ~2.1 Å for Cu(II)-N) to the size of secondary building blocks (~6.5 × 6.5 × 6.7 $Å^3$ for $[Cd_8(TAZ)_9]$ and ~6.2 × 6.2 × 6.3 $Å^3$ for $[Cu_8(TAZ)_9]$), and to the final MOF pore (~5.5 Å for SNNU-98-Cd and ~5.1 Å for SNNU-98-Cu). Rational and hyperfine pore control together with optimized Lewis basic N sites endow SNNU-98-M with benchmark multi-scenario CO_2 capture performance varying from binary flue gas (CO_2/N_2) to ternary biogas ($CO_2/CH_4/N_2$) and even to quinary coal gas ($CO_2/CH_4/N_2/CO/H_2$) mixtures by a one-step process. Low-cost raw materials, easy scalablity in synthesis, ultra-high stability, top-level selective adsorption ability as well as multi-scenario adaptability make SNNU-98-Cu ideal carbon capture material for practical applications.

Introduction

With CO_2 emissions projected to exceed 500 ppm by 2050, the removal of greenhouse gases from dilute emissions has been identified as one of the seven chemical separations that will change the world.[1-5] Currently, CO_2 removal scenarios can be mainly divided into pre-combustion capture (biogas $CO_2/CH_4/N_2$ and coal gas $CO_2/CH_4/N_2/CO/H_2$), post-combustion capture (flue gas CO_2/N_2), and direct air capture.[6-12] The conventional amine scrubbing method is widely used for CO_2 capture, but the absorbent regeneration consumes a large amount of energy and requires additional waste treatment process.[13, 14]

Physical adsorption is recognized as a promising carbon capture method due to its high efficiency, easy operation, non-corrosive, and low energy consumption.[15-18] A large variety of adsorbents, including zeolites, porous carbon materials, porous organic networks have been explored and applied in CO_2 removal.[19, 20] From an application perspective, the construction of highly CO_2 selective adsorbents suitable for multi-scenarios such as flue gas, biogas, and coal gas is extremely necessary but remains a challenging task.[3] As a new type of adsorbent, metal-organic framework (MOF) has the ability to rationally regulate the thermodynamic and kinetic processes and is considered as an ideal platform for developing the next generation of CO_2 capture materials.[5, 21] Up to now, most adsorbents are explored to deal with a single separation process[22] and the development of MOFs for multi-scenario carbon capture is urgent.

Due to the highly similar physical properties and tiny molecular size difference (usual sub-Ångstrom level, Table S1†) of involved gas molecules, ultrafine pore regulation is important for multi-scenario carbon capture MOF adsorbent design. However, a sub-Ångstrom pore size regulation in typical MOFs containing metal clusters and inter-cluster organic linkers is not easy although the iso-network principle and building block approach have achieved remarkable success.[23] And some other common strategies including organic linker functionalization[24-27], framework penetration[28] and pore space partition[29] also seem powerless to solve this problem. In our opinion, the main reason for this situation is that the presence of inter-cluster organic linkers. Their minor variations (e.g., addition or removal of a single atom) can induce pore size fluctuations exceeding 1 Å significantly surpassing the sub-Ångstrom-level structural control. On the other hand, the flexibility of inter-cluster linkers may also reduce the variations in coordination bond lengths between different metal centers, resulting in nearly identical pore sizes for isostructural MOFs containing distinct metals (Scheme 1a).

Based on the above considerations, an inter-cluster-linker-absence-enabled sub-Ångstrom pore modulation strategy is proposed herein (Scheme 1b). The removal of inter-cluster linkers will generate architectures consisting of clusters directly connected to clusters[30-32], which well combines the advantages of inorganic zeolites and MOFs with extra-high stability.

Key Laboratory of Applied Surface and Colloid Chemistry (MOE), Key Laboratory of Macromolecular Science of Shaanxi Province, School of Chemistry & Chemical Engineering, Shaanxi Normal University, Xi'an, Shaanxi, 710062, China. E-mail: zhaiqg@snnu.edu.cn

† Electronic supplementary information (ESI) available. CCDC 2416690. For ESI and crystallographic data in CIF or other electronic format see DOI: 10.1039/x0xx00000x

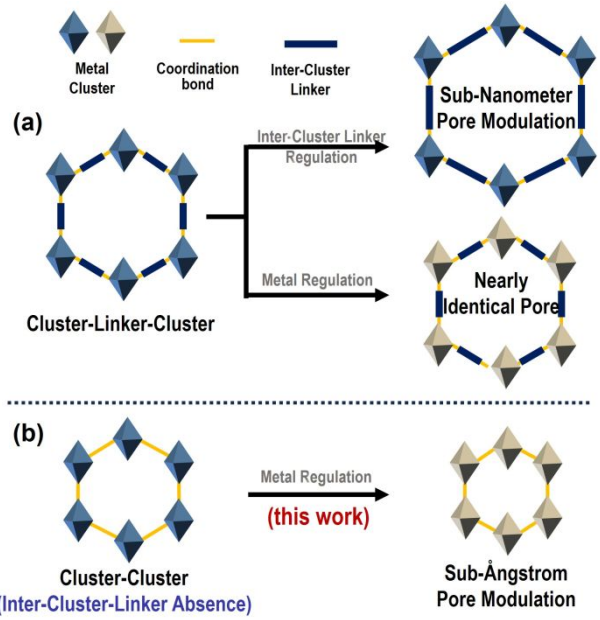

Scheme 1. The inter-cluster-linker-absence-enabled sub-Ångstrom pore modulation strategy proposed in this work.

What's more important is that ultra-fine pore regulation can be achieved just by replacing the metal nodes, which may successfully transmit the sub-Ångstrom level changes of coordination bond length to the whole pore environment.

The feasibility of this strategy is well-demonstrated in SNNU-98-M MOF materials composed of directly-connected $[M_8(TAZ)_9]$ (M = Cd or Cu, TAZ = tetrazolate) triangular prism clusters. Due to the ionic radius of Cu^{2+} (0.73 Å) are significantly smaller than that of Cd^{2+} (0.95 Å), the absence of inter-cluster linkers effectively transfers the difference from coordination bond length to the size of secondary building blocks and to the final MOF pore capture (~5.5 Å for SNNU-98-Cd and ~5.1 Å for SNNU-98-Cu). Benefited from this sub-Ångstrom pore modulation, SNNU-98-Cu adsorbent sets a benchmark for challenging multi-scenario CO_2 capture ability with ultrahigh CO_2/N_2 (flue gas) selectivity (1509.3), top-level separation of ternary $CO_2/CH_4/N_2$ ternary mixtures (biogas, breakthrough interval time of 9 min g^{-1} for N_2, 18.3 min g^{-1} for CH_4, and 80.9 min g^{-1} for CO_2), and even highly efficient one-step CO_2 capture from a quinary coal gas ($CO_2/CH_4/N_2/CO/H_2$) mixtures, outperforming all advanced materials. Meanwhile, the removal of inter-cluster linkers from SNNU-98-Cu also led to a superb acid and alkali resistance stability, which can be stable in pH = -0.5-13 solutions for 7 days, and in pH = 1-12 solutions for as long as half a year surpassing almost all highly stable MOF materials. In addition, rapid, efficient, and low energy consumption reflux synthesis route endow SNNU-98-Cu adsorbents with great potential for large-scale production and commercialization.

Results and discussion

The typical solvothermal reactions of low-cost metal salts and tetrazole ligands produced isostructural SNNU-98-M metal-organic frameworks[33, 34] with a formula of $[M_5(TAZ)_9(NO_3)\cdot(H_2O)_n]$ (M = Cd^{2+}/Cu^{2+}, TAZ = tetrazolate). SNNU-98-Cu can be scaled up by an ultra-fast and efficient reflux synthesis process. Only 30 min refluxing reaction of raw materials at 150 °C can produce 10.8 g of SNNU-98-Cu with a high yield of about 85% (Figure 1 and Figure S2-S3). Powder X-ray diffraction (PXRD) patterns and scanning electron microscopy (SEM) images confirmed the high purity and high crystallinity of SNNU-98-Cd/Cu (Figure S1-S3 and Table S2†) obtained by two different synthesis methods.

Single crystal structure analysis indicates that the framework of SNNU-98-Cd/Cu is formed by the direct connection of triangular prism clusters without inter-cluster organic linkers. Specifically, different metal centers result in a gap of about 0.2 Å in the metal-N coordination bond lengths (Cd(II)-N of ~2.3 Å and Cu(II)-N of ~2.1 Å) (Figure 1a and 1b). Eight metals are connected through six μ_3-TAZs and three μ_4-TAZs to form $[M_8(TAZ)_9]$ clusters. The difference in metal-N bond lengths further rationally resulted in a bulk reduction of $[Cu_8(TAZ)_9]$ cluster (~6.2 × 6.2 × 6.3 $Å^3$) compared to $[Cd_8(TAZ)_9]$ cluster (~6.5 × 6.5 × 6.7 $Å^3$) (Figure 1c and 1d). Each $[M_8(TAZ)_9]$ cluster connects with six equal adjacent neighbors through vertex (metal) sharing patterns to generate a 3D structure with typical *acs* topology.[35] Due to the removal of inter-cluster linkers, the lattice of the 3D framework formed by $[M_8(TAZ)_9]$ cluster stacking contracted by the substitution of metallic cadmium with copper, and the *c*/*a* ratio of cell size decreased by about 1% (Figure 1e and 1f). Such ultrafine changes of coordination bond length ultimately transmit to the one-dimensional hexagonal channel and successfully achieved a sub-Ångstrom-level modulation (~5.5 Å for SNNU-98-Cd and ~5.1 Å for SNNU-98-Cu) (Figure 1g and 1h).

The permanent porosity and sub-Ångstrom pore modulation of activated SNNU-98-Cd/Cu materials was confirmed by N_2 (77 K) and CO_2 (195 K) adsorption and desorption isotherms. As shown in Figure 2a, SNNU-98-Cd exhibits a type I adsorption isotherm, while SNNU-98-Cu almost does not adsorb N_2 at 77 K. Further, CO_2 adsorption experiments at 195 K show their permanent microporosity and reversible type I adsorption isotherms (Figure 2b) with calculated Brunauer-Emmett-Teller (BET) surface areas of 322 $m^2\ g^{-1}$ (SNNU-98-Cd) and 212 $m^2\ g^{-1}$ (SNNU-98-Cu). The pore size distributions of SNNU-98-Cd/Cu are calculated to be 5.1 Å and 4.8 Å, further confirming the ultra-fine pore size control, which also highly matched with their single crystal structure. Clearly, the removal of inter-cluster linkers can successfully transmit the coordination bond length gap and rationally achieve sub-Ångstrom pore regulation.

Thermal and chemical stability has long been a limitation of MOF materials towards industrial applications, especially for multi-scenario CO_2 capture. The unique structural features may endow SNNU-98-Cd/Cu with ulra-high stability: (i) soft-base N sties and soft-acidic metal sites can form strong coordination bond; (ii) tetrazolate anions with lower pKa value can significantly promote the acid resistance; (iii) the absence of inter-cluster linkers will improve the robustness of MOF framework. Thermogravimetric analysis (TGA) of the synthesized and methanol-exchanged samples showed that SNNU-98-Cd/Cu both has good thermal stability (Figure S4†).

View Article Online
DOI: 10.1039/D5SC02144H

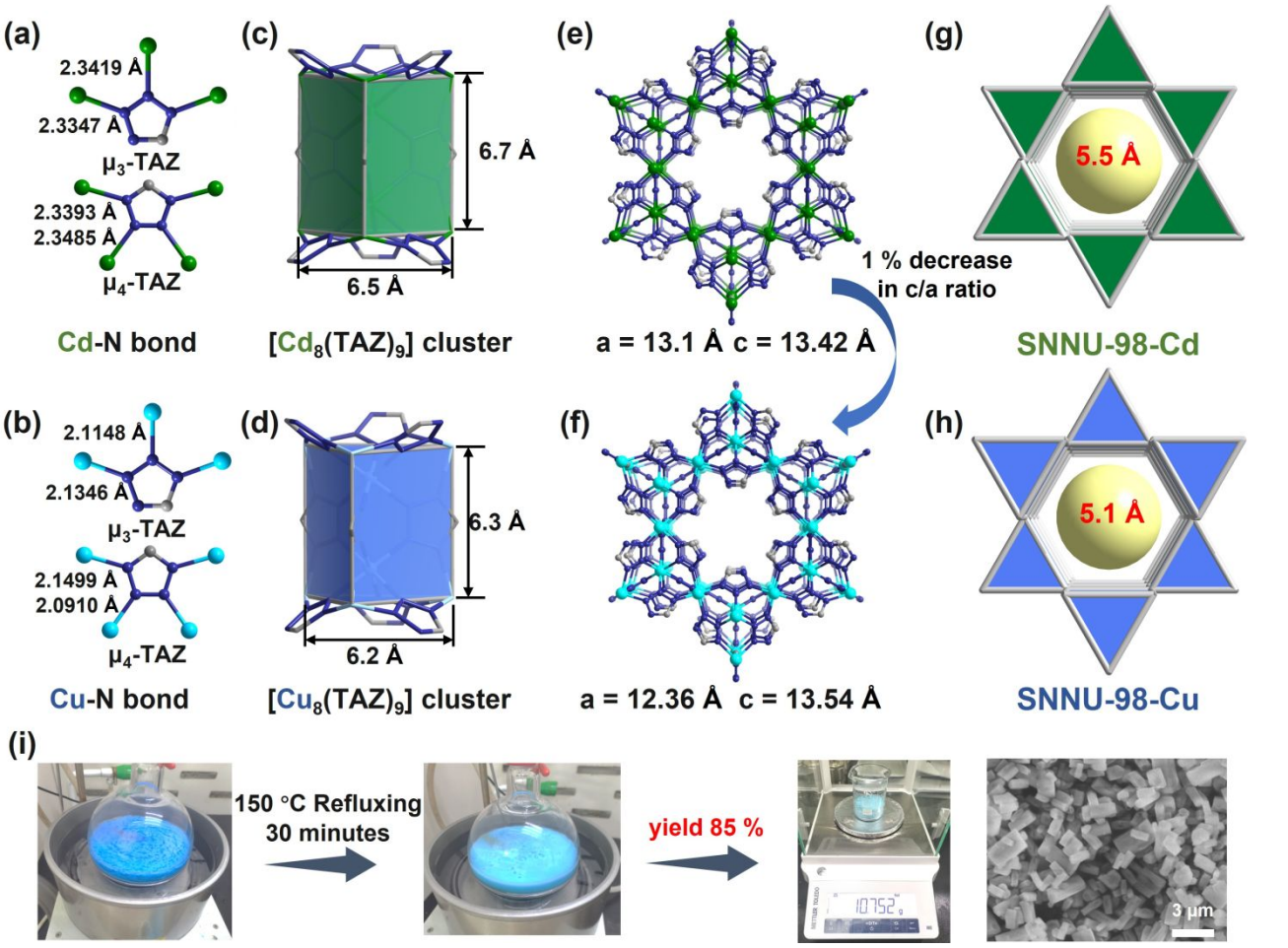

Figure 1. Illustration of the structures and rapid reflux synthesis route of SNNU-98-Cd/Cu MOFs: (a and b) comparison of metal-N bond lengths; (c and d) detailed comparison of $[Cd_8(TAZ)_9]$ and $[Cu_8(TAZ)_9]$ clusters; (e, f, j and h) detailed comparison of 3D porous frameworks and 1D hexagonal channel viewed along the c-axis direction; (i) scale-up production of SNNU-98-Cu material.

Furthermore, SNNU-98-Cu was immersed in pH = 1-14 and 1-3 M HCl solutions to test its acid-base stability. PXRD results showed that SNNU-98-Cu remained highly crystalline for up to 7 days in pH = -0.5-13 solutions (Figure 2c). Encouragingly, it can still remain stable until 6 months (pH = 1-12), which is an extraordinarily long stability surpassing almost all MOF adsorbent materials. The pH stability range and duration of SNNU-98-Cu are better than all reported Cu-MOFs , most well-known highly-stable MOFs, such as UiO-66[36], ZIF-8[37], MOF-808[38] and even most of the recognized Zr-MOFs[39-41] with high degree of connectivity (Table S3† and Figure S5-S7†). In addition, the 195 K CO_2 adsorption of SNNU-98-Cu after the acid-base stability test showed that the structure still maintains a high degree of crystallinity and intact pore structure (Figure 2d and 2e). Among them, the adsorption capacity remained unchanged after 6 months of immersion in pH = 12 solution, and the pore size distribution changed slightly, suggesting that the pore structure may have undergone a subtle collapse, but the effect on the overall gas adsorption performance was neglectable. Low-cost raw materials, rapid scale-up reflux synthesis, and ultra-high stability make SNNU-98-Cu able to cope with the complex environment of industrial CO_2 capture process.

The CO_2, CH_4, and N_2 adsorption of SNNU-98-Cd/Cu was investigated at different temperatures (Figure S8-S13† and Table S8-S9†) to systematically evaluate the effect of sub-Ångstrom pore regulation on selective CO_2 capture. As shown in Figure 3a, the CO_2 adsorption of SNNU-98-Cu (124.1 cm^3 cm^{-3}) is higher than that of SNNU-98-Cd (109.1 cm^3 cm^{-3}) at 298 K and 1 bar. In addition, SNNU-98-Cu (80.1 cm^3 cm^{-3}, 64.5% at 1 bar) exhibits superior CO_2 adsorption than SNNU-98-Cd (42.5 cm^3 cm^{-3}, 38.9% at 1 bar) at relatively low pressure (0.15 bar) and 298 K, which outperforming most of the well-known MOF adsorbents, such as SIFSIX-2-Cu-i[42] (58.9 cm^3 cm^{-3}), NJU-Bai8[43] (38.1 cm^3 cm^{-3}), and Qc-5-Cu-sql[14] (24.4 cm^3 cm^{-3}) (Figure 3b). Obviously, the adjustment of ultra-fine pore size, resulting in SNNU-98-Cu with more suitable narrow pores and high density uncoordinated tetrazolate N sites suitable for rapid mass adsorption of CO_2. In contrast, the CH_4 and N_2 uptakes on SNNU-98-Cd/Cu at 298 K and 1 bar were found to be only 37/24 cm^3 cm^{-3} and 8.4/6.2 cm^3 cm^{-3}, illustrating the molecular-sieving effect of SNNU-98-Cd/Cu. Similarly, the same adsorption characteristics were observed at 273 and 283 K (Figure S10†).

View Article Online
DOI: 10.1039/D5SC02144H

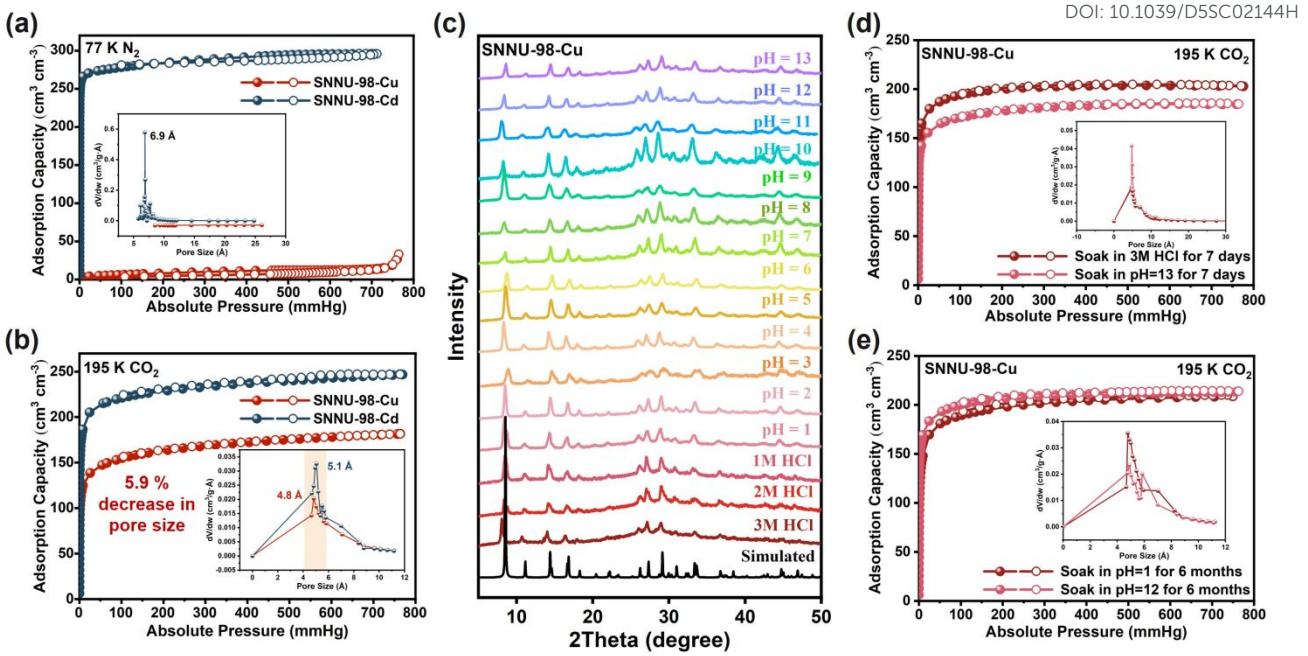

Figure 2. Stability and porosity of SNNU-98-Cd/Cu MOFs: (a) 77 K N_2 adsorption and calculated pore size distributions; (b) 195 K CO_2 adsorption and calculated pore size distributions; (c) PXRD patterns of SNNU-98-Cu immersed in pH = -0.5-13 solution for 1 week; (d and e) 195 K CO_2 adsorption curves and calculated pore size distributions of SNNU-98-Cu after immersed in -0.5-13 solution for 1 week and pH = 1-12 solution for 6 months.

Furthermore, the separation ratios of CO_2 versus CH_4 and N_2 of SNNU-98-Cu (5.2/20) were significantly higher than those of SNNU-98-Cd (2.9/13), suggesting that the pore size sub-Ångstrom reduction can favor the multi-scene CO_2 separation (Figure 3c). Notably, SNNU-98-Cd/Cu could still maintain the original adsorption amount after multiple CO_2 adsorption and desorption, indicating a good cyclic stability (Figure 3d and Figure S13†).

Heat of adsorption (Q_{st}) of CO_2, CH_4, and N_2 were further calculated based on the adsorption isotherms at different temperatures to understand the binding affinities between host surface and guest gas molecules (Figures S14-S17† and Table S4-S5†). At zero coverage, the $-Q_{st}$ values of CO_2, CH_4, and N_2 are 34.6, 20.8, and 25.9 kJ mol^{-1} for SNNU-98-Cu and 25.2, 28.6, and 35.7 kJ mol^{-1} for SNNU-98-Cd, respectively (Figure 3g). The CO_2 adsorption affinity of SNNU-98-Cu was significantly stronger than that of SNNU-98-Cd. And the CO_2 affinity was also higher than that of CH_4 and N_2 in SNNU-98-Cu, which indicated that SNNU-98-Cu had a greater potential for CO_2 capture and separation. Notably, the $-Q_{st}$ value of SNNU-98-Cu was maximum at zero loading, whereas the $-Q_{st}$ calue of SNNU-98-Cd gradually increased with adsorption, which could be attributed to the smaller pore environment with stronger affinity for CO_2 at low pressure, which is consistent with the adsorption performance. In addition, compared with other well-known CO_2 separation materials, SNNU-98-Cu has a moderate CO_2 adsorption enthalpy, which is favorable for recycling in practical applications (Table S10†). The CO_2 temperature-programmed desorption (CO_2-TPD) curves also showed that the CO_2 desorption temperature and thermal conductivity detector (TCD) intensity of SNNU-98-Cu (123 °C) were higher than those of SNNU-98-Cd (94 °C), indicating its stronger binding with CO_2 (Figure S18†).

The separation potentials of SNNU-98-Cd/Cu for CO_2/N_2, CO_2/CH_4, and CH_4/N_2 mixtures were evaluated by ideal adsorbed solution theory (IAST) (Figure S19–S27† and Table S6-S7†). For CO_2/N_2 (15/85, *v/v*), the selectivity values of SNNU-98-Cd/Cu at 298 K and 1 bar were 70.1 and 1509.3, respectively (Figure 3e). The ultra-high selectivity value of SNNU-98-Cu exceeds most of top-level MOF adsorbents, such as ZU-301[10] (846), MUF-16[6, 15] (631), NJU-Bai52[44] (581), and UTSA-16[45] (314.7). The IAST selectivity values are of 8.5/94.6 for CO_2/CH_4 (50/50, *v/v*) and 6.5/5.3 for CH_4/N_2 (50/50, *v/v*) at 298 K and 1 bar (Figure 3f and S21†). These values further indicate that SNNU-98-Cu has a greater potential to separate multi-scenario CO_2 (Figure 3h). In particular, when considering the adsorption and separation selectivity of CO_2, the comprehensive capacity of SNNU-98-Cu is superior to most benchmark MOF adsorbents, such as ZU-36-Ni[4], NMMOF-9a[3], and ZU-66[8] (Figure 3i).

To evaluate the feasibility of the actual multi-scenario CO_2 separation process, dynamic fixed-bed breakthrough experiments were further conducted for the binary gas mixtures including flue gas (CO_2/N_2) and CO_2/CH_4, ternary biogas ($CO_2/CH_4/N_2$) and quinary coal gas ($CO_2/CH_4/N_2/CO/H_2$) (Figure 4 and Figures S28–S35†). For the CO_2/N_2 (15/85, v/v) flue gas separation, N_2 was first observed from the column due to the lower adsorption capacity and weak affinity with the MOF frameworks, whereas CO_2 was not eluted until the breakthrough interval time reached 64.4 min g^{-1} for SNNU-98-Cd and 82.6 min g^{-1} for SNNU-98-Cu with a flow rate of 2 mL min^{-1} at 298 K (Figure 4a). Excitingly, CO_2 can be retained in the column over 109.8 min g^{-1} and 127.1 min g^{-1} at 273 K for SNNU-98-Cd and SNNU-98-Cu (Figure S28†).

View Article Online
DOI: 10.1039/D5SC02144H

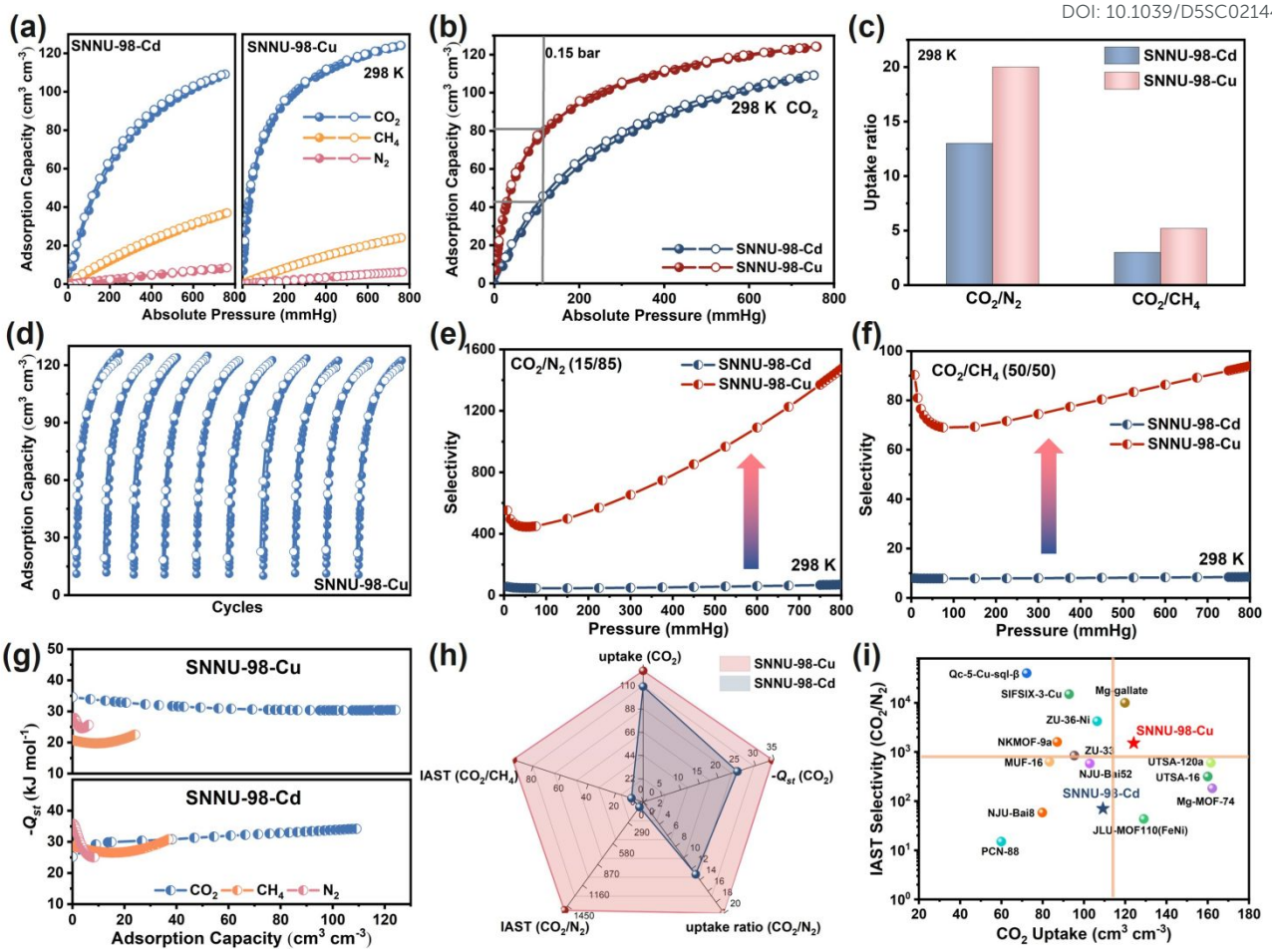

Figure 3. Static adsorption performance of SNNU-98-Cd/Cu: (a) CO_2, CH_4, and N_2 adsorption isotherms at 298 K; (b) CO_2 adsorption isotherms at 298 K and 0.15 bar; (c) CO_2/N_2 and CO_2/CH_4 uptake ratio at 298 K; (d) CO_2 adsorption cycle stability of SNNU-98-Cu; (e and f) comparison of CO_2/N_2, and CO_2/CH_4 selectivity at 298 K; (g) heat of adsorption values of CO_2, CH_4, and N_2; (h) radar plots comparing the adsorption performance regulated by the pore modulation; (i) summary of IAST (CO_2/N_2) and the CO_2 uptake among reported top-level MOF adsorbents.

Notably, these breakthrough interval time values are superior to almost all MOF adsorbents up to now under the same conditions, such as UTSA-120a (80 min g^{-1}), JLU-MOF110(FeNi)[2] (49.1 min g^{-1}), and ZU-66[8] (28 min g^{-1}) and only lower than ZU-301[10] (175 min g^{-1}) and FJI-H29[7] (114 min g^{-1}). In addition, the interval time of SNNU-98-Cu was longer than that of SNNU-98-Cd (18.2 min g^{-1}) indicating that the sub-Ångstrom pore modulation is conducive to the separation of flue gas components. Subsequently, the separation effect of SNNU-98-Cu on the CO_2/N_2 mixed gas remained unchanged in humid environment (50% and 98% RH), indicating that it has great potential for industrial applications (Figure S29†). The cyclic stability of CO_2/N_2 were tested, which further demonstrated the accuracy and reproducibility of the separation performance of SNNU-98-Cu (Figure S32†). It is noted that the breakthrough time did not decrease proportionally with increasing flow rate (Figure 4b), which may be due to the strong interaction between SNNU-98-Cu adsorbent and CO_2 molecules. The high CO_2 adsorption at low-pressure also indicates that the separation of CO_2/N_2 (15/85, v/v) in SNNU-98-Cu mainly dominated by thermodynamics. The superb flue gas separation effect of SNNU-98-Cu was attributed to a clear thermodynamic effect that CO_2 had a higher affinity for the high-density N sites of the pores in a narrower pore environment.

As for the binary biogas separation CO_2/CH_4 (50/50, v/v), the CH_4 was first observed from the column, whereas CO_2 was not eluted until the breakthrough interval time reached 29 min g^{-1} for SNNU-98-Cd and 31 min g^{-1} for SNNU-98-Cu with a flow rate of 2 mL min^{-1} at 298 K (Figure 4c). The interval time of SNNU-98-Cu was almost the same as that of SNNU-98-Cd, but the outflow time was much earlier (CH_4: 12, 27 min g^{-1}, CO_2: 43, 56 min g^{-1}). This may be due to the kinetic diffusion effect of SNNU-98-Cu is greater than the thermodynamic effect, resulting in the preferential outflow in SNNU-98-Cu. Furthermore, the CO_2/CH_4 separation performance is also better than most of the MOF materials, especially considering the materials for simultaneous separation of flue gas and biogas, SNNU-98-Cu is almost superior to all high-performance MOFs, second only to ZU-301[10] (Figure 4d and Table S11†).

View Article Online
DOI: 10.1039/D5SC02144H

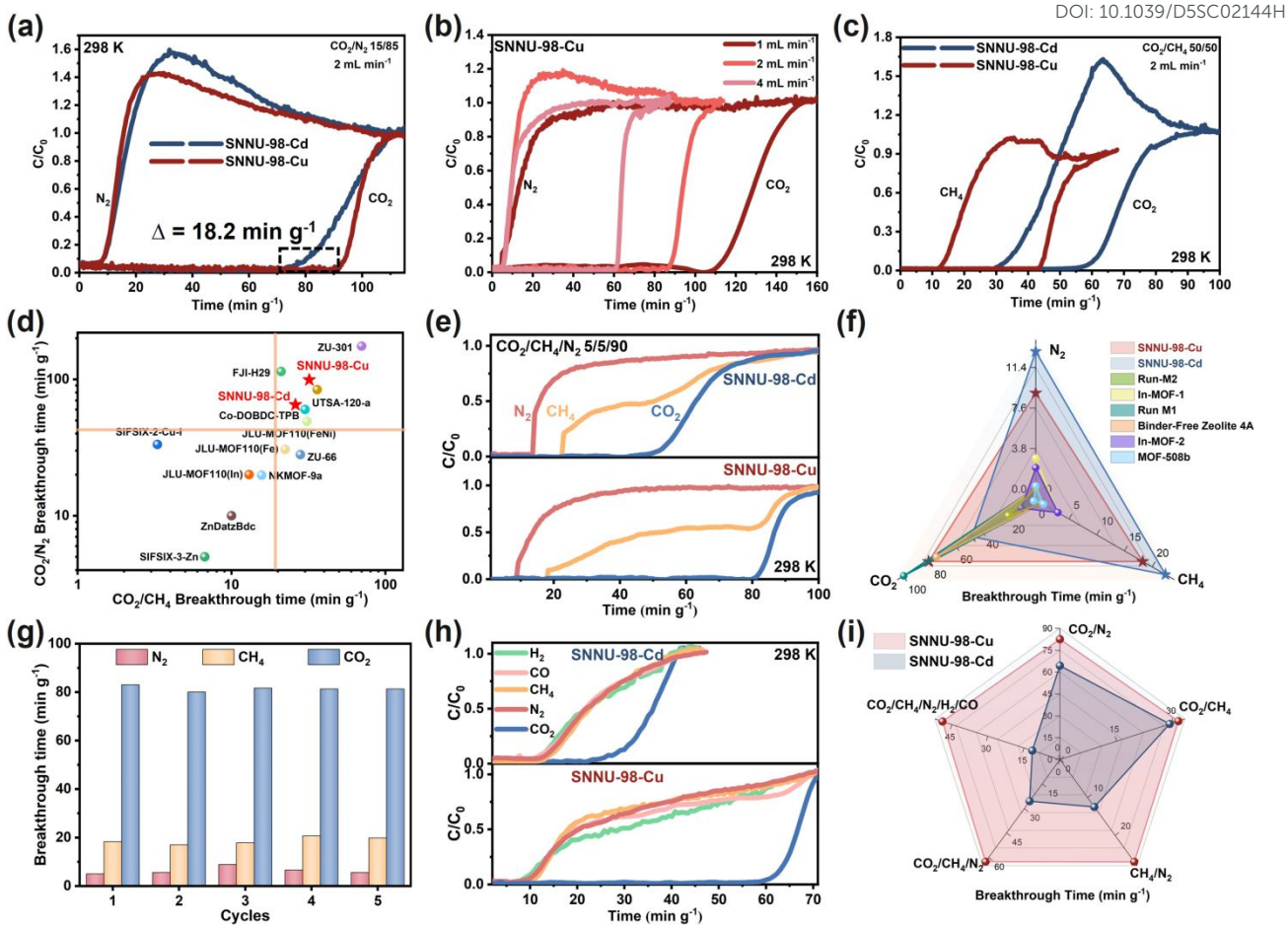

Figure 4. The experimental breakthrough separation performance for SNNU-98-Cd/Cu: (a and c) breakthrough curves for CO_2/N_2 (15/85, v/v) and CO_2/CH_4 (50/50, v/v) gas mixtures at 298 K and 1 bar; (b) breakthrough curves for CO_2/N_2 (15/85, v/v) gas mixtures of SNNU-98-Cu at different flow rates; (d) summary of CO_2/N_2 against CO_2/CH_4 breakthrough interval times for top-level MOFs at 298 K; (e) breakthrough curves for $CO_2/CH_4/N_2$ (5/5/90, v/v/v) gas mixtures at 298 K and 1 bar; (f) comparison of $CO_2/CH_4/N_2$ three-component separation properties of currently studied MOF materials; (g) cyclicing breakthrough tests for $CO_2/CH_4/N_2$ (5/5/90, v/v/v) on SNNU-98-Cu; (h) experimental breakthrough curves for $N_2/CO_2/CO/CH_4/H_2$ (66.3/14.5/9.1/5/5.1, v/v/v/v/v) gas mixtures at 298 K and 1 bar; (i) radar plots illustrating the practical separation performance regulated by the pore modulation.

In addition, it also has a great advantage for the difficult problem of CH_4/N_2 (10/90, v/v) separation. The N_2 was first observed from the column, whereas CH_4 was not eluted until the breakthrough interval time reached 12.5 min g^{-1} for SNNU-98-Cd and 27 min g^{-1} for SNNU-98-Cu (2 mL min^{-1} at 298 K) (Figure S31†).

Multi-component gas separation plays an important role in adsorption separation technology, but it is still in the initial stage. The separation of ternary biogas mixture $CO_2/CH_4/N_2$ (5/5/90, v/v/v) was firstly evaluated. As shown in Figure 4e, N_2 and CH_4 broke through the adsorption column at 12.9 and 22.4 min g^{-1}, whereas CO_2 was not detected at the exit until 47.9 min g^{-1} for SNNU-98-Cd. Notably, the shrinking of pore size produced much better performance with the outflow of N_2 detected at 9 min g^{-1}, while the outflow of CH_4 and CO_2 from the column was 18.3 and 80.9 min g^{-1}, respectively. Such separation of $CO_2/CH_4/N_2$ ternary gas mixture in a single process is unprecedented, and the separation ability is further promoted as the temperature decreases, which is superior to all adsorbent materials attempting to this separption process (Figure 4f and Table S12†). Notably, the CH_4 breakthrough curve shows a plateau region in the middle stage, which is due to the presence of competing adsorption. Simultaneous adsorption and desorption of CH_4 occurs until CO_2 adsorption is saturated , and then the C/C_0 rises to 1 at the same time. In addition, this three-component separation has excellent cyclic stability (Figure 4g). Subsequently, real industrial separation ratios ($CO_2/CH_4/N_2$: 30/65/5 and 40/55/5, v/v/v) of SNNU-98-Cu were further simulated, which showed that N_2 broke through at 6 min g^{-1} , CH_4 at 23 and 29 min g^{-1} , respectively, while CO_2 was not detected until 88 and 80 min g^{-1}. It further confirmed that SNNU-98-Cu has great potential for industrial applications (Figure S34).

View Article Online
DOI: 10.1039/D5SC02144H

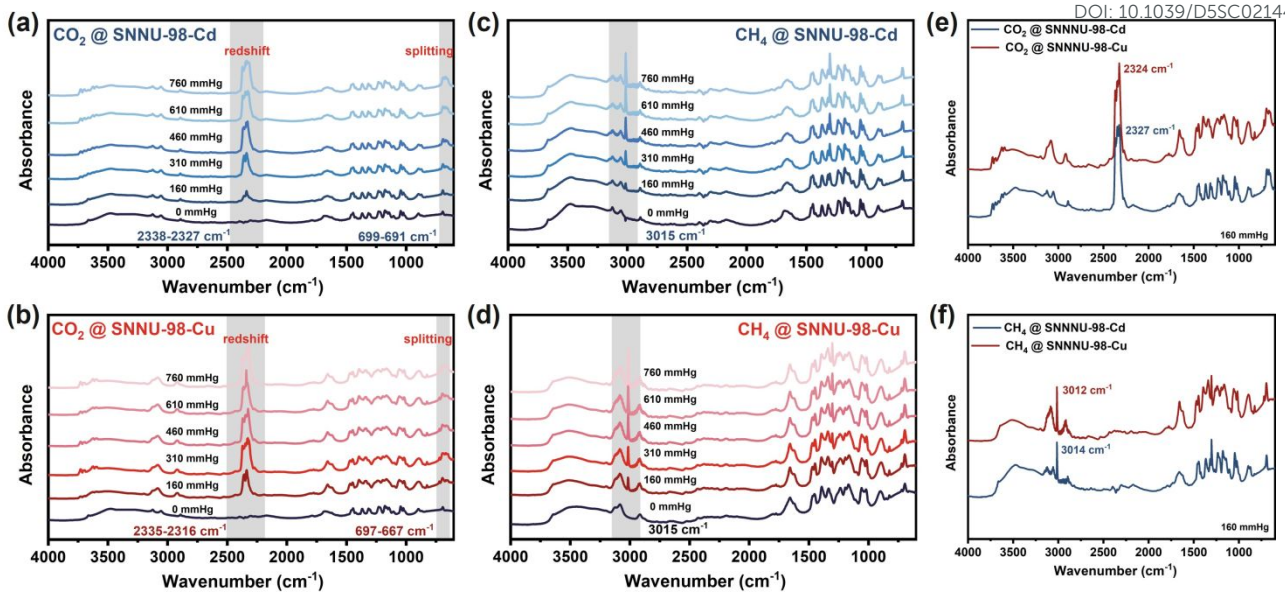

Figure 5. In situ FT-IR spectra of SNNU-98-Cd/Cu: (a and b) for CO_2 adsorption process; (c and d) for CH_4 adsorption process; (e and f) comparison of CO_2 and CH_4 adsorption.

Furthermore, the adsorption capacities were calculated from the breakthrough curves and compared with single-component gas adsorption (Table S13† and S14†). The results showed that the low-pressure CO_2 breakthrough capacity of SNNU-98-Cu was higher than that of SNNU-98-Cd. For CO_2/N_2 (15/85, v/v) at 298 K, the CO_2 adsorption capacity of SNNU-98-Cu/Cd was calculated to be 56.9 and 64.6 $cm^3\ cm^{-3}$ compared to 41.2, 80 $cm^3\ cm^{-3}$ for static adsorption, respectively. This is also consistent with GCMC simulation and -Q_{st} values, which further confirms that SNNU-98-Cu has a good separation effect.

To further demonstrate the multi-scenario adaptability of SNNU-98-Cd/Cu adsorbents, the low calorific value coal gas with a practical composition of $N_2/CO_2/CO/H_2O/CH_4/H_2$ (58.4/14.5/9.1/8/5.1/4.8, v/v/v/v/v/v) was selected. Extraordinarily, SNNU-98-Cd/Cu can realize efficient one-step CO_2 capture from this five-component gas mixture (Figure 4h). The N_2, CO, CH_4, and H_2 gas components concurrently broke through the adsorption column at 10 min g^{-1}, whereas CO_2 was not detected at the exit until 21.5 and 58.9 min g^{-1} for SNNU-98-Cd and SNNU-98-Cu. Notably, SNNU-98-Cd/Cu also possessed high water vapor adsorption capacity (Figure S36†), which further indicated that these rubust MOFs without inter-cluster linkers may cope with complex industrial separation scenario and achieve unprecedented separation results. Overall, benefited from an inter-cluster-linker-absence-enabled sub-Ångstrom pore modulation, SNNU-98-Cu shows much better comprehensive CO_2 capture ability than SNNU-98-Cd (Figure 4i). The ultra-microporous environments coupled with high density of bare tetrazolate N sites leads to strongest interactions with CO_2 molecules and achieving efficient multi-scenario separation in a thermodynamic and kinetic synergy.

In situ infrared (IR) spectroscopic measurements further probed the interaction of the SNNU-Cd/Cu with CO_2 and CH_4, whereas the N_2 molecule has a high degree of symmetry and absorbs IR light very weakly (Figure 5 and Figure S37-S38†). The results show that the CO_2 asymmetric telescopic vibrational peaks (v_3 = 2349 cm^{-1}) are red-shifted and the bending vibrational peaks (v_2 = 667 cm^{-1}) are split, which proves that CO_2 interacts strongly with SNNU-98-Cd/Cu. As shown in Figure 5a and 5b, CO_2-loaded SNNU-98-Cu (2335-2316 cm^{-1}) is red-shifted more than SNNU-98-Cd (2338-2327 cm^{-1}). The peak position differences of SNNU-98-Cd/Cu bending vibrational peak splitting were 8 cm^{-1} and 30 cm^{-1}, and the vibrational peaks of SNNU-98-Cu at 3000-3250 cm^{-1} were significantly stronger than those of SNNU-98-Cd, indicating a stronger C-H···O_{CO2} interaction between SNNU-98-Cu and CO_2. On the other hand, with the increase of pressure, the characteristic peak of CH_4-loaded SNNU-98-Cd/Cu appeared at 3015 cm^{-1}, and it gradually enhanced (Figure 5c and 5d). The spectra of CO_2 and CH_4 at low pressure indicate that the peaks of SNNU-98-Cu are stronger than those of SNNU-98-Cd, which further proved that SNNU-98-Cu had much stronger affinity with CO_2 and CH_4 (Figure 5e and 5f). All these results not only validate above adsorption separation performance, but also illustrate the power of sub-Ångstrom pore modulation on the multi-scenario CO_2 capture.

To further insight into the host–guest interactions and adsorption behavior at the molecular level, Grand Canonical Monte Carlo (GCMC) simulations were performed. As shown in Figure 6, SNNU-98-Cd and SNNU-98-Cu obviously adsorb different amounts of gas molecules in a certain channel, at 298 K and 1 bar. SNNU-98-Cu adsorbed significantly more CO_2 molecules than SNNU-98-Cd, and the amount of CO_2 exceeded that of CH_4 and N_2, indicating that CO_2 has stronger interaction in smaller pores. This is very useful for efficient capturing CO_2 from multiple industrial scenarios.

View Article Online
DOI: 10.1039/D5SC02144H

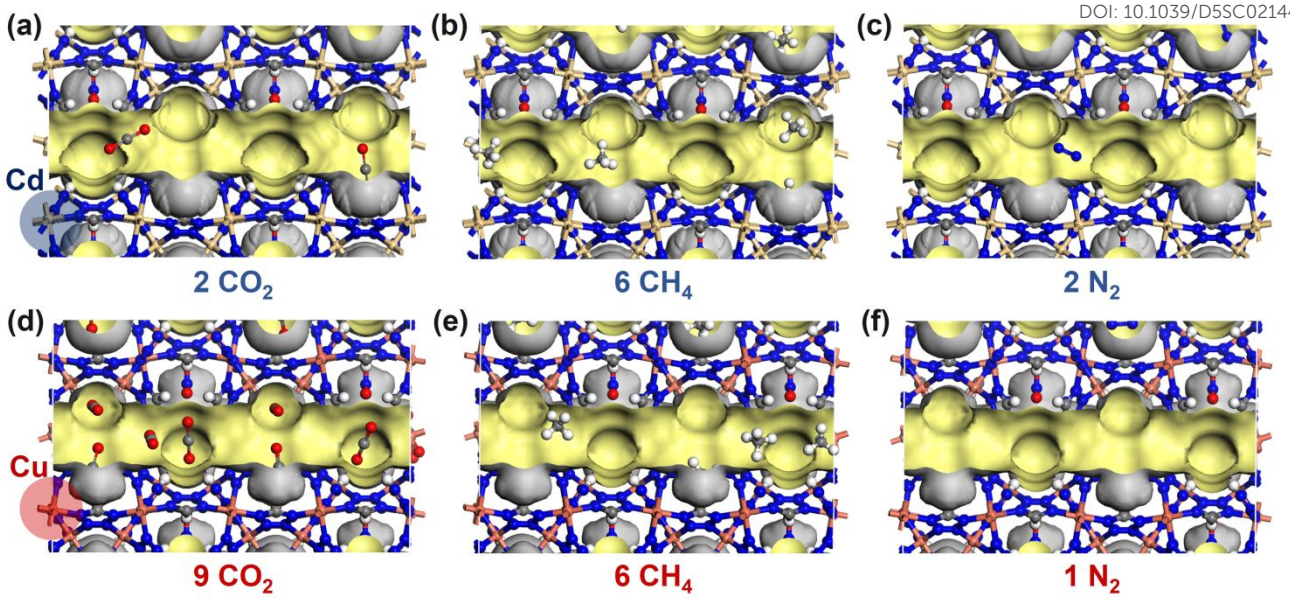

Figure 6. GCMC simulated CO_2 (a and d), CH_4 (b and e) and N_2 (c and f) distributions in the channel of SNNU-98-Cd/Cu MOFs.

As shown in Figure S39†, the binding sites of CO_2 mainly interacts with high-density bare tetrazolate N sites and hydrogen bond with H, where SNNU-98-Cu (N···C_{CO2}: 2.7861-3.6808 Å, C-H···O_{CO2}: 2.3646-3.108 Å) interacts significantly stronger than SNNU-98-Cd (N···C_{CO2}: 3.6063-3.9138 Å, C-H···O_{CO2}: 2.8270-3.4154 Å), thus can adsorb more CO_2 molecules. It is confirmed that the reduced pore size at the Ångstrom level enhances the interaction between the framework and CO_2. On the other hand, CH_4 molecules with larger kinetic diameters have weaker N···H-C_{CH4} interactions with N atoms in the pores (2.9424-3.8830 Å for SNNU-98-Cd, 2.5317-3.0746 Å for SNNU-98-Cu). This indicates that CH_4 diffuses more slowly in the micropores, and SNNU-98 can separate CO_2 and CH_4 efficiently by kinetic sieving. In addition, the polarizability and quadrupole moment of N_2 are lower than those of CO_2, and thus the interaction with SNNU-98-Cu (H···N_{N2}: 2.8799-3.8322 Å) and SNNU-98-Cd (H···N_{N2}: 2.5857-3.9138 Å) is weaker, suggesting an excellent separation of CO_2 and N_2 based on thermodynamic principles. Subsequently, the density distributions of different gas molecules were further calculated, which clearly showed that the interaction between CO_2 and SNNU-98-Cd/Cu adsorbents was stronger than those of CH_4 and N_2. And the CO_2 distribution density in SNNU-98-Cu was significantly higher than that of SNNU-98-Cd, especially in the low-pressure region (Figure S40-S44†). This further demonstrate that CO_2 has stronger interaction in smaller pores, thereby benchmarked capturing CO_2 in multiple scenarios (flue gas, biogas, and coal gas).

Conclusions

In summary, this work proposes a rational sub-Ångstrom pore modulation strategy for metal-organic frameworks by the removal of inter-cluster linkers. With the absence of inter-cluster linkers, tiny changes in coordination bond lengths triggered by metal regulation can be efficiently transmitted, enabling ultra-fine pore size control and further significantly promote the multi-scenario CO_2 capture performance. Due to the suitable pore environment and high density of bare N sites, SNNU-98-Cu exhibits ultra-high stability (pH = -0.5-13), top-level CO_2/N_2 selectivity (1509.3), and best CO_2 capture ability superior to nearly all porous adsorbent material, which can efficiently separate CO_2 from binary flue gas, ternary biogas and quinary coal gas mixtures in one step. In situ IR spectra and GCMC calculations clearly indicate that the benchmark CO_2 capture performance is due to the coupling effect of thermodynamics and dynamics in the ultra-micropore space. In general, this work introduces a valid strategy realizing hyperfine pore size regulation of MOF adsorbent and prompts the CO_2 capture from "single-scene passive adaptation" to "multi-scene active response", which may provide a combination of high efficiency, economy and sustainability for industrial carbon emission reduction.

Author contributions

Q.-G. Z. and J.-W. W. conceived the idea of this research. J.-W. W. carried out the experiments, analyzed the results and wrote the manuscript. Q.-G. Z. led the project and edited the manuscript and edited the manuscript. All authors participated in and contributed to the preparation of the manuscript.

Conflicts of interest

There are no conflicts to declare.

Data availability

All the associated data are available in the ESI.†

Acknowledgements

This work was financially supported by the National Natural Science Foundation of China (22471149), the Youth Innovation Team of Shaanxi Universities (2023), and the Fundamental Research Funds for the Central Universities (GK202307009).

Notes and references

1 L. Zhang, Z. He, Y. Liu, J. You, L. Lin, J. Jia, S. Chen, N. Hua, L.-A. Ma, X. Ye, Y. Liu, C.-X. Chen and Q. Wang, *ACS Appl. Mater. Interfaces*, 2023, **15**, 30394-30401.
2 W. Li, X. Liu, X. Yu, B. Zhang, C. Ji, Z. Shi, L. Zhang and Y. Liu, *Inorg. Chem.*, 2023, **62**, 18248-18256.
3 S. Geng, H. Xu, C.-S. Cao, T. Pham, B. Zhao and Z. Zhang, *Angew. Chem. Int. Ed.*, 2023, **62**, e202305390.
4 Z. Zhang, Q. Ding, S. B. Peh, D. Zhao, J. Cui, X. Cui and H. Xing, *Chem. Commun.*, 2020, **56**, 7726-7729.
5 F. Chen, J. Wang, L. Guo, X. Huang, Z. Zhang, Q. Yang, Y. Yang, Q. Ren and Z. Bao, *Sep. Purif. Technol.*, 2022, **292**, 121031.
6 O. T. Qazvini and S. G. Telfer, *ACS Appl. Mater. Interfaces*, 2021, **13**, 12141-12148.
7 D. Wu, C. Liu, J. Tian, F. Jiang, D. Yuan, Q. Chen and M. Hong, *Inorg. Chem.*, 2020, **59**, 13542-13550.
8 L. Yang, X. Cui, Y. Zhang, Q. Wang, Z. Zhang, X. Suo and H. Xing, *ACS Sustain. Chem. Eng.*, 2019, **7**, 3138-3144.
9 A. Pal, S. Chand, S. M. Elahi and M. C. Das, *Dalton Trans.*, 2017, **46**, 15280-15286.
10 C. Yu, Q. Ding, J. Hu, Q. Wang, X. Cui and H. Xing, *Chem. Eng. J.*, 2021, **405**, 126937.
11 J.-R. Li, J. Yu, W. Lu, L.-B. Sun, J. Sculley, P. B. Balbuena and H.-C. Zhou, *Nat. Commun.*, 2013, **4**, 1538.
12 Z. Zhou, T. Ma, H. Zhang, S. Chheda, H. Li, K. Wang, S. Ehrling, R. Giovine, C. Li, A. H. Alawadhi, M. M. Abduljawad, M. O. Alawad, L. Gagliardi, J. Sauer and O. M. Yaghi, *Nature*, 2024, **635**, 96-101.
13 O. Shekhah, Y. Belmabkhout, Z. Chen, V. Guillerm, A. Cairns, K. Adil and M. Eddaoudi, *Nat. Commun.*, 2014, **5**, 4228.
14 K.-J. Chen, D. G. Madden, T. Pham, K. A. Forrest, A. Kumar, Q.-Y. Yang, W. Xue, B. Space, J. J. Perry, J.-P. Zhang, X.-M. Chen and M. J. Zaworotko, *Angew. Chem. Int. Ed.*, 2016, **55**, 10268-10272.
15 O. T. Qazvini, R. Babarao and S. G. Telfer, *Nat. Commun.*, 2021, **12**, 197.
16 Q. Shi, *J. Fuel Chem. Technol.*, 2021, **49**, 1531-1539.
17 D. Song, S. Zou, Z. Ji, Y. Li, H. Li, Y. Zhou, C. Chen, Q. Chen and M. Wu, *Angew. Chem. Int. Ed.*, 2025, **64**, e202423496
18 Z. Wang, Y. Zhang, E. Lin, S. Geng, M. Wang, J. Liu, Y. Chen, P. Cheng and Z. Zhang, *J. Am. Chem. Soc.*, 2023, **145**, 21483-21490.
19 L. F. A. S. Zafanelli, A. Henrique, M. Karimi, A. E. Rodrigues and J. A. C. Silva, *Ind. Eng. Chem. Res.*, 2020, **59**, 13724-13734.
20 B. Li, S. Wang, Z. Tian, G. Yao, H. Li and L. Chen, *Adv. Theory Simul.*, 2022, **5**, 2100378.
21 E. Aly, L. F. A. S. Zafanelli, A. Henrique, M. Golini Pires, A. E. Rodrigues, K. Gleichmann and J. A. C. Silva, *Ind. Eng. Chem. Res.*, 2021, **60**, 15236-15247.
22 E. Wu, X.-W. Gu, D. Liu, X. Zhang, H. Wu, W. Zhou, G. Qian and B. Li, *Nat. Commun.*, 2023, **14**, 6146.
23 X. Feng, X. Wang, H. Yan, H. Liu, X. Liu, J. Guan, Y. Lu, W. Fan, Q. Yue and D. Sun, *Angew. Chem. Int. Ed.*, 2024, **63**, e202407240.
24 J. Wang, Y. Zhang, Y. Su, X. Liu, P. Zhang, R.-B. Lin, S. Chen, Q. Deng, Z. Zeng, S. Deng and B. Chen, *Nat. Commun.*, 2022, **13**, 200.
25 S. Yuan, L. Huang, Z. Huang, D. Sun, J.-S. Qin, L. Feng, J. Li, X. Zou, T. Cagin and H.-C. Zhou, *J. Am. Chem. Soc.*, 2020, **142**, 4732-4738.
26 W. Fan, X. Zhang, Z. Kang, X. Liu and D. Sun, *Coord. Chem. Rev.*, 2021, **440**, 213968.
27 S. Yuan, Y.-P. Chen, J.-S. Qin, W. Lu, L. Zou, Q. Zhang, X. Wang, X. Sun and H.-C. Zhou, *J. Am. Chem. Soc.*, 2016, **138**, 8912-8919.
28 H.-L. Jiang, T. A. Makal and H.-C. Zhou, *Coord. Chem. Rev.*, 2013, **257**, 2232-2249.
29 Y. Ye, Z. Ma, R.-B. Lin, R. Krishna, W. Zhou, Q. Lin, Z. Zhang, S. Xiang and B. Chen, *J. Am. Chem. Soc.*, 2019, **141**, 4130-4136.
30 J.-W. Wang, S.-C. Fan, Z. Li, Q.-Q. Zhang, Y.-F. Zhang, Z.-Y. Wang, W. Yuan, Y. Wang and Q.-G. Zhai, *Adv. Funct. Mater.*, 2024, **35**, 2420070.
31 S. P. Chan and Y. Zhang, *Chem. Eur. J.*, 2023, **29**, e202301279.
32 Q.-G. Zhai, C.-Z. Lu, S.-M. Chen, X.-J. Xu and W.-B. Yang, *Cryst. Growth Des.*, 2006, **6**, 1393-1398.
33 Z.-J. Hou, Z.-Y. Liu, N. Liu, E.-C. Yang and X.-J. Zhao, *Dalton Trans.*, 2015, **44**, 2223-2233.
34 J.-W. Wang, S.-C. Fan, H.-P. Li, X. Bu, Y.-Y. Xue and Q.-G. Zhai, *Angew. Chem. Int. Ed.*, 2023, **62**, e202217839.
35 Z. Chen, P. Li, R. Anderson, X. Wang, X. Zhang, L. Robison, L. R. Redfern, S. Moribe, T. Islamoglu, D. A. Gómez-Gualdrón, T. Yildirim, J. F. Stoddart and O. K. Farha, *Science*, 2020, **368**, 297-303.
36 M. Kandiah, M. H. Nilsen, S. Usseglio, S. Jakobsen, U. Olsbye, M. Tilset, C. Larabi, E. A. Quadrelli, F. Bonino and K. P. Lillerud, *Chem. Mater.*, 2010, **22**, 6632-6640.
37 K. Leus, T. Bogaerts, J. De Decker, H. Depauw, K. Hendrickx, H. Vrielinck, V. Van Speybroeck and P. Van Der Voort, *Microporous Mesoporous Mater.*, 2016, **226**, 110-116.
38 W. Liang, H. Chevreau, F. Ragon, P. D. Southon, V. K. Peterson and D. M. D'Alessandro, *CrystEngComm*, 2014, **16**, 6530-6533.
39 H. Yang, F. Peng, A. N. Hong, Y. Wang, X. Bu and P. Feng, *J. Am. Chem. Soc.*, 2021, **143**, 14470-14474.
40 H.-L. Jiang, D. Feng, K. Wang, Z.-Y. Gu, Z. Wei, Y.-P. Chen and H.-C. Zhou, *J. Am. Chem. Soc.*, 2013, **135**, 13934-13938.
41 Y. Duan, H. Li, X. Shi, C. Ji, J. Imbrogno and D. Zhao, *Ind. Eng. Chem. Res.*, 2025, **64**, 5372-5382.
42 P. Nugent, Y. Belmabkhout, S. D. Burd, A. J. Cairns, R. Luebke, K. Forrest, T. Pham, S. Ma, B. Space, L. Wojtas, M. Eddaoudi and M. J. Zaworotko, *Nature*, 2013, **495**, 80-84.
43 L. Du, Z. Lu, K. Zheng, J. Wang, X. Zheng, Y. Pan, X. You and J. Bai, *J. Am. Chem. Soc.*, 2013, **135**, 562-565.
44 X. Song, M. Zhang, C. Chen, J. Duan, W. Zhang, Y. Pan and J. Bai, *J. Am. Chem. Soc.*, 2019, **141**, 14539-14543.
45 S. Xiang, Y. He, Z. Zhang, H. Wu, W. Zhou, R. Krishna and B. Chen, *Nat. Commun.*, 2012, **3**, 954.

View Article Online
DOI: 10.1039/D5SC02144H

Data Availability Statement

All the associated data are available in the supporting information.